

1 **High-resolution epigenome analysis in nasal samples derived from children with respiratory**
2 **viral infections reveals striking changes upon SARS-CoV-2 infection**

3

4 Konner Winkley¹, Boryana Koseva¹, Dithi Banerjee², Warren Cheung¹, Rangaraj Selvarangan^{2*},
5 Tomi Pastinen^{1*}, Elin Grundberg^{1*}

6

7 ¹Department of Pediatrics, Genomic Medicine Center, Children's Mercy Kansas City, Kansas
8 City, Missouri, US.

9 ²Department of Pathology and Laboratory Medicine, Children's Mercy Kansas City, Kansas City,
10 Missouri, US.

11

12 *Corresponding authors: Elin Grundberg, PhD (egrundberg@cmh.edu); Tomi Pastinen, MD, PhD
13 (tpastinen@cmh.edu); Rangaraj Selvarangan (rselvarangan@cmh.edu)

14

15 **Abstract**

16 Background: DNA methylation patterns of the human genome can be modified by
17 environmental stimuli and provide dense information on gene regulatory circuitries. We
18 studied genome-wide DNA methylation in nasal samples from infants (<6 months) applying
19 whole-genome bisulfite sequencing (WGBS) to characterize epigenome response to 10 different
20 respiratory viral infections including SARS-CoV-2.

21 Results: We identified virus-specific differentially methylated regions (vDMR) with human
22 metapneumovirus (hMPV) and SARS-CoV-2 followed by Influenza B (Flu B) causing the weakest

23 vs. strongest epigenome response with 496 vs. 78541 and 14361 vDMR, respectively. We found
24 a strong replication rate of FluB (52%) and SARS-CoV-2 (42%) vDMR in independent samples
25 indicating robust epigenome perturbation upon infection. Among the FluB and SARS-CoV-2
26 vDMRs, around 70% were hypomethylated and significantly enriched among epithelial cell-
27 specific regulatory elements whereas the hypermethylated vDMRs for these viruses mapped
28 more frequently to immune cell regulatory elements, especially those of the myeloid lineage.
29 The hypermethylated vDMRs were also enriched among genes and genetic loci in monocyte
30 activation pathways and monocyte count. Finally, we perform single-cell RNA-sequencing
31 characterization of nasal mucosa in response to these two viruses to functionally analyze the
32 epigenome perturbations. Which supports the trends we identified in methylation data and
33 highlights and important role for monocytes.

34 Conclusions: All together, we find evidence indicating genetic predisposition to innate immune
35 response upon a respiratory viral infection. Our genome-wide monitoring of infant viral
36 response provides first catalogue of associated host regulatory elements. Assessing epigenetic
37 variation in individual patients may reveal evidence for viral triggers of childhood disease.

38 **Key words:**

39 DNA methylation, infant, influenza, viral infection, GWAS, SARS-CoV-2

40

41

42

43

44

45 **Background**

46 Methylation of cytosine bases in the CpG context plays an important role in controlling gene
47 expression and can be modified by environmental and biological stimuli. This has led to
48 methylation patterns being studied in many contexts including complex disease (Allum et al.
49 2019; Liang et al. 2015), infection (Maeda et al. 2017; Matsusaka et al. 2017; Mcerlean et al.
50 2014), and developmental processes (Smith et al. 2012; Okano et al. 1999). A key analysis in
51 these studies is the identification of which genomic regions change in methylation level in
52 response to the stimulus of interest. We and others have shown that variable and disease-
53 associated DNA methylation regions map to regulatory regions, specifically enhancers
54 (Grundberg et al. 2013; Allum et al. 2015). These differentially methylated regions (DMRs)
55 provide information about pathways that may be activated or suppressed in response to
56 environmental stimuli (Busche et al. 2015; Tsaprouni et al. 2014). Because of this, whole
57 genome bisulfite sequencing (WGBS) - the gold standard method for assessing genome-wide
58 DNA methylation at single base resolution - can provide genome-scale insight into the
59 mechanism of action for biological phenomenon.

60 The COVID-19 pandemic has led to a dramatic surge in research on the host response
61 mechanisms to respiratory virus infection, specifically in response to SARS-CoV-2 infection.
62 However, there are several other respiratory viruses beyond SARS-CoV-2 that are known to
63 cause acute respiratory illness (ARI), and there are still gaps in knowledge about the interplay
64 between the host immune system and viral replication in many if not all of these viruses. While
65 these viruses are evolutionarily distant (Stec et al. 1991; Collins et al. 2013; Lu et al. 2020), the
66 clinical presentation of illness from their infection is quite similar. It is therefore unknown if

67 these viruses are more similar to, or more divergent from one another in the host immune
68 responses they illicit upon infection. Additionally, there are viruses such as Respiratory Syncytial
69 Virus (RSV), that are known to cause a significant burden of acute lower respiratory infection
70 episodes in children under the age of five specifically (Shi et al. 2017). Because these first few
71 months of life are a critical time period for immune system development, and immune
72 responses during this time are strikingly different from the response to similar pathogens later
73 in life (Zhang et al. 2017; Ygberg and Nilsson 2012), we set out to map the host nasal
74 epigenome response through WGBS to respiratory viral infection in infants across ten different
75 viruses including SARS-CoV-2. Because we will measure epigenome changes in the direct tissue
76 of infection, this data would give us genome-wide insights into the regulatory circuitries
77 involved in the host antiviral response, and potentially allow us to identify sources of variation
78 leading to inter-individual differences in infection. This dataset would also allow us to identify
79 pathways that are shared amongst groups of viruses, as well as virus-specific methylation
80 changes. To this end, we link almost 20 million CpGs to viral response and map biological
81 function of viral-associated CpGs within functional elements. We highlight that different
82 respiratory viruses vary in the magnitude and direction of the alterations they cause to the host
83 epigenome, perhaps reflecting differential immunogenicity. We note that SARS-CoV-2 and
84 Influenza B (FluB) cause the largest magnitude of change and show similar differential
85 methylation profiles. We show the robustness of epigenome perturbation upon SARS-CoV-2
86 and FluB infection through replication in independent and age-matched nasal samples. We
87 further use single-cell RNA-sequencing as well as GWAS data to functionally validate these

88 methylation changes and find evidence for a signature of monocyte insufficiency that may be a
89 predisposition to infection or increased viral replication by FluB and SARS-CoV-2.

90 **Results**

91 Methylation signatures in infant nasal epigenomes upon respiratory viral infections

92 We generated WGBS data on 11 pools of nasal samples collected from children (<6 months)
93 with one of the 10 respiratory viruses and age-matched non-infected infants presented at the
94 hospital with ARI (Table 1). Where available, each sample consisted of a pool of equimolar
95 amount of individual DNA with the following infection status and sample size: 1) N=10
96 Adenovirus (Adeno), 2) N=10 Coronavirus OC43 (Corona OC43), 3) N=5 Enterovirus D68
97 (EVD68), 4) N=10 Influenza Type A (FluA), 5) N=10 Influenza Type B (FluB), 6) N=10 Human
98 metapneumovirus (hMPV), 7) N=10 Human Parainfluenza Virus Type 3 (PIV3), 8) N=5
99 Respiratory syncytial virus (RSV), 9) N=10 Rhinovirus/enterovirus (REV) and 10) N=1 SARS-CoV-
100 2. In addition, two pools of non-infected (NI) samples were generated (Table 1).

101 Table 1: Cohort characteristics

Virus Type	N	Mean age (months)	SD
Adeno	10	3.4	2.2
Corona Oc43	10	1.9	1.9
EVD68	5	2.8	1.6
FluA	10	3.5	1.8
FluB	10	4.0	1.3
hMPV	10	2.8	1.8
PIV3	10	2.4	1.9
RSV	5	2.5	2.3
RV (REV)	10	2.0	2.2
SARS-CoV-2	1	1.0	-
Negative-1	5	6.6	2.7

102
103 Each pool was sequenced at high depth (~22.5X unique read coverage) identifying on average
104 25 million CpGs per pool, each at >10X (Supplementary Table 1) of which 19.2 million CpGs

105 were covered across all samples. These data sets were then used to cluster the samples
106 hierarchically using correlation distances (Figure 1). SARS-CoV-2 signatures appear to have the
107 largest distance to all other respiratory viral signatures. Among the nine other signatures, FluB,
108 FluA, and EVD68 were distinctive from the remaining six data sets, where additional sub-
109 structure was observed in the clustering.

110 Next, we computed genome-wide methylation differences in virus-positive vs. matched
111 negative control samples by applying Fisher's exact test of methylated vs unmethylated reads
112 at CpG sites with at least 10 reads in both the pooled viral sample and the negative control.

113 Consecutive nominally significant CpGs ($p < 0.01$) were grouped ($N \geq 3$) together into
114 differentially methylated regions based on viral infection (vDMR) when having the same
115 direction of effect and within 250bp of the adjacent CpG. For comparisons to the background
116 nasal epigenome, we repeated the differential methylation calculations using two sets of
117 negative control sets keeping the significance and grouping criteria the same.

118 Using these criteria, focusing on virus-positive vs. matched negative controls, we noted striking
119 differences in vDMRs (Supplementary Table 2) across respiratory viruses as outlined in Figure
120 2A. In fact, the vDMR discovery rates follow a similar pattern as shown in the clustering
121 analysis. Specifically, SARS-CoV-2 and FluB are associated with the strongest host response
122 signature with SARS-CoV-2 as a clear outlier with almost 80000 vDMRs.

123 We then divided the vDMRs per virus type into hypermethylated or hypomethylated as a
124 potential indication of deactivation/suppression vs. activation of regulatory circuitries upon
125 viral infection, respectively. We noted that a subset of the respiratory viruses (EVD68, FluA,
126 RSV, FluB and SARS-CoV-2) had the majority (60-70%) of their vDMRs being hypomethylated

127 pointing towards significant activation of regulatory elements upon infection (Figure 2B).
128 Indeed, regulatory element annotation showed that the hypomethylated vDMRs from not only
129 EVD68, FluA, FluB and SARS-CoV-2 but also PIV3 and Adeno, were significantly more likely to
130 map to epithelial-specific regulatory elements compared to the background control (1.5-2.5-
131 fold, Supplementary Figure 1A) (Fisher's Exact Test, Bonferroni $p < 6.25E-4$). In fact, only hMPV,
132 CoronaOC43, REV, and RSV hypo vDMR did not significantly deviate from the background
133 control potentially indicating a milder activation of the respiratory epithelium (Supplementary
134 Figure 1A). On the other hand, RSV hypomethylated vDMR were significantly (Fisher's $P = 9.4E-$
135 15) enriched within immune-specific regulatory elements. Specifically, we found a striking
136 overrepresentation (Fisher's $P = 5.67E-20$) of lymphoid-specific regulatory elements among RSV
137 hypomethylated vDMR (Supplementary Figure 2). This observation is in line with recent
138 evidence showing elevated levels of Type 2 respiratory innate lymphoid cells in infants with RSV
139 infection (Norlander and Peebles 2020).

140 Next we annotated the hypermethylated vDMR and found in general a different pattern than
141 for hypomethylated. For Adeno, EVD68, FluA, FluB and SARS-CoV-2, hypermethylated vDMRs
142 were significantly enriched (Fisher's Exact Test, Bonferroni $p < 6.25E-4$) among immune-specific
143 elements. This indicates deactivation or insufficiency of immune cell regulatory machineries in
144 the host as a consequence or causing a viral infection/replication (Supplementary Figure 1B).

145 Robust epigenome perturbation upon FluB and SARS-CoV-2 infection

146 We further evaluated the two viruses (FluB and SARS-CoV-2) causing the strongest epigenome
147 response in the host and gathered additional age-matched samples derived from infants: 1)
148 N=5 non-infected controls (average age 2.2 months), N=3 FluB (average age 6 months) and N=1

149 SARS-CoV-2 (average age 9 months). Each pool was again sequenced at high depth (~35X
150 unique read coverage) (Supplementary Table 1).

151 We first repeated the vDMR analysis (using parameters listed above) using the age-matched
152 negative control samples and overlapped the results with the discovery FluB and SARS-CoV-2
153 vDMRs, respectively. We considered a vDMR to be replicated if at least one CpG per vDMR
154 overlapped and the same direction of methylation change upon infection was observed in both
155 discovery and replication vDMR, respectively (Supplementary Table 3).

156 Using this conservative threshold, we found 52% (N=7516) and 42% (N=32,318) of the vDMRs
157 to be replicated for FluB and SARS-CoV-2, respectively. Additionally, the genome wide
158 methylation profiles of the discovery and replicate datasets clustered together when
159 considering the top 50% of variable CpGs, demonstrating the reproducibility of the epigenomic
160 perturbations (Figure 1). Then, we extended the replication analysis by querying the
161 methylation levels of all the discovery vDMRs from the replication set (N=14361 and N=78542
162 vDMRs for FluB and SARS-CoV-2). We noted high correlation in the SARS-CoV-2 ($r=0.79$)
163 (Supplementary Figure 3A) whereas similar analysis of the FluB vDMR showed a weaker
164 correlation across data sets ($r=0.4$) (Supplementary Figure 3B) supporting the notion that
165 COVID-19 is associated with strong epigenome effects in the host.

166 FluB and SARS-CoV-2 hypermethylation and lack of activation of the innate immune system

167 Similar to the pattern for all vDMR (Supplementary Figure 1), we found that the FluB and SARS-
168 CoV-2 replicated hypomethylated vDMR were more likely to map to epithelial-specific
169 regulatory elements (Figure 3A) than the background control (Fisher's $p=6.59E-29$ and $p=2.43E-$
170 17 for FluB and SARS-CoV-2) whereas the hypermethylated vDMRs were enriched among

171 immune cell specific regulatory elements (Fisher's $p=1.11E-24$ and $p=1.72E-23$ for FluB and
172 SARS-CoV-2). We further disentangled these immune-cell specific signatures by separating
173 regulatory elements specific to myeloid and lymphoid lineages as well as those shared across
174 immune cells. We noted clear differences across immune cell lineages where the observed
175 signature among hypermethylated vDMR was driven by regulatory elements specific to myeloid
176 cells only (Figure 3B-C). In all, these results indicate a striking virus-induced activation of the
177 epithelial-specific gene regulatory machinery but a deactivation of regulation of myeloid cells or
178 an alternative absence of myeloid cells.

179 Additionally, we queried genes associated with the vDMRs specific to FluB and SARS-CoV-2,
180 respectively, in GREAT (5.0 kb upstream and downstream for a single nearest gene) and found
181 leukocyte mediated immunity as the most significant biological process associated with these
182 hypermethylated vDMRs ($p=1.5E-8$, Supplementary Figure 4).

183 Next, we used the Flu B and SARS-CoV2-specific hypermethylated vDMRs to identify potential
184 enrichment of transcription factor binding sites (TFBS) (see Methods) to understand which
185 regulatory pathways are associated with these viral infections. As expected, given the
186 magnitude of vDMRs in SARS-CoV-2 vs. FluB comparisons, we found almost twice as many
187 enrichments in SARS-CoV-2 vs FluB hyper vDMR at nominal $p < 0.01$ ($N=145$ vs $N=74$,
188 Supplementary Table 4-5). We performed Gene Ontology (GO) term enrichment analysis of
189 TFBS enrichments at $P < 10^{-10}$ which corresponded to 50 and 22 unique TF genes for SARS-CoV-2
190 and FluB, respectively, with a 100% overlap of FluB TF genes among the SARS-CoV-2 genes.
191 Among these GO biological processes annotations, myeloid cell differentiation was the top
192 enriched term ($P=5.12E-13$, Supplementary Table 6) potentially indicating absence of sufficient

193 activation of the innate immune system and thus increased viral replication. In fact, the top
194 enriched TFBS for both SARS-CoV-2 and FluB hyper vDMR corresponded to *ELF4* ($p=1E-208$ and
195 $p=1E-51$; Supplementary Table 4-6) which is known to be critical for antiviral immunity and host
196 defense by activating innate immunity (You et al. 2013; Szabo and Rajnavolgyi 2014). We
197 examined the expression pattern of *ELF4* across hematopoietic cells using publicly available
198 data (Stunnenberg et al. 2016) and found highest expression in cells of the myeloid lineage
199 (Supplementary Figure 5).

200 Functional analysis of replicated vDMR in childhood infection

201 To investigate the functional roles of the replicated vDMRs for both FluB and SARS-CoV-2, we
202 performed single-cell RNA-sequencing (scRNAseq) on pooled nasal mucosal samples from
203 children infected with Flu B ($n=4$, average age = 6.25 years), SARS-CoV-2 ($n=3$, average age =
204 7.66 years), and from uninfected and age-matched controls ($n=5$, average age = 7 years). We
205 captured and sequenced over 12,000 cells across the pools (FluB = 3,687 cells, SARS-CoV-2 =
206 2,864 cells, control = 4,963 cells), and were able to identify all expected major cell types (Figure
207 4A).

208 We examined the expression level of gene “modules” consisting of those genes within 5 kb of a
209 replicated vDMR for FluB and SARS-CoV-2. First, we observed that the gene modules associated
210 with hypomethylated vDMRs for FluB and SARS-CoV-2 are more highly expressed in epithelial
211 cell types than in immune cell types (Figure 4B-B’). Interestingly, the gene modules associated
212 with hypermethylated vDMRs for FluB and SARS-CoV-2 are more highly expressed in immune
213 cell types than epithelial cell types, thus corroborating our previous cellular annotations of

214 vDMRs (Figure 4C-C'). In fact, we observed the largest increase of expression of these genes
215 after infection in monocytes (Figure 4C).

216 In an attempt to clarify if the observed hypermethylation of myeloid associated genomic
217 regions was a consequence of infection or represented a potential absence of myeloid cells
218 which functions as an epigenetic predisposition to infection or increased viral replication, we
219 examined the activity of myeloid cells after infection in both FluB as well as SARS-CoV-2. We
220 hypothesized that if the observed hypermethylation of myeloid regulatory genomic regions was
221 a consequence of viral infection, we should see a decrease in either cell number or activity of
222 myeloid cells compared to controls. We found that the proportion of myeloid cells was not
223 fundamentally changed after either viral infection compared to controls (Figure 4D). To assess
224 myeloid cell activity after infection, we quantified the number of cell-cell interactions through
225 ligand receptor pairs. We found that monocytes had the largest number of interactions with
226 other cell types after both FluB and SARS-CoV-2 infection (Figure 4E) and were consistently
227 increased in their cell-cell interactions compared to controls after infection in both SARS-CoV-2
228 and FluB (Supplementary Figure 6). These results together indicate that myeloid cell activity
229 and proportion in the nasal mucosa is not decreased as a result of FluB or SARS-CoV-2 infection,
230 but rather an environmental or genetic predisposition to a viral infection and replication due to
231 insufficient resident myeloid cells in the nasal mucosa may be the cause for the observed
232 hypermethylation of myeloid regulatory regions as opposed to active immune suppression by
233 viral infection.

234 Virus-associated hypermethylation overlap disease loci

235 To test the hypothesis of a potential genetic predisposition, we used genetic loci identified in
236 large-scale genome-wide association studies (GWAS) to guide our interpretation of the
237 biological consequences of these environmentally perturbed epigenome variations. With the
238 observed enrichment of myeloid immune cellular pathways among the hypermethylated
239 pattern in regulatory elements associated with both FluB and SARS-CoV-2, and the lack of
240 functional evidence for myeloid cell suppression in the scRNAseq data, we naturally opted to
241 utilize genetic information linked to human blood cell trait variation identified from a large
242 meta-analysis of GWAS to test our hypothesis that resident myeloid cell absence may be a
243 predisposition for FluB and SARS-CoV-2 infection. Specifically, we integrated common genetic
244 loci associated with hematological traits from the largest GWAS to date identifying almost
245 17000 genetic variants across 28 blood cell phenotypes (Vuckovic et al. 2020). We assessed the
246 co-localization of these variants within the 7516 and 32318 Flu B and SARS-CoV-2 vDMR and
247 contrasted similar co-localization pattern within randomly selected control regions matching
248 the genomic contexts of the vDMR (N=49623). We performed Fisher's Exact test to evaluate the
249 difference in proportional overlap in test (vDMRs) vs. control regions, respectively. Intriguingly,
250 we found monocyte proportion as the most significant trait both for hypermethylated FluB
251 (Fisher P=4.85E-5) and hypermethylated SARS-CoV-2 vDMR (Fisher P 1.06E-8), respectively
252 (Supplementary Figure 7, Supplementary Table 7)), indicating that observed interindividual
253 variation in susceptibility to viral infections may have a genetic basis.

254 **Discussion**

255 We have demonstrated the breadth of host epigenomic alterations occurring in infants in
256 response to 10 common respiratory viruses during childhood including SARS-CoV-2. We find

257 that while there is substantial variability in the magnitude of methylome response to different
258 viral infections, many of the identified DMRs are reproducibly identifiable between
259 independent infections, indicating robust epigenome response to infection. Additionally, we
260 demonstrate an important role for innate cells, specifically monocytes, in the antiviral response
261 to influenza B and SARS-CoV-2.

262 While our functional analysis of vDMR for FluB and SARS-CoV-2 through scRNAseq confirms
263 that genes near hypomethylated vDMR do increase in expression after infection, the converse
264 was not true for hypermethylated vDMRs. Typically, hypermethylation is interpreted as a
265 repression of the specific genomic region involved. However, an alternative explanation is that
266 a heterogenous cell population contains fewer cells of the lineage associated with a specific
267 regulatory region. Given that genes near hypermethylated vDMRs for FluB and SARS-CoV-2
268 actually increase in expression after infection, that these hypermethylated vDMRs are enriched
269 for regions that are associated with monocyte development, and that monocyte activity
270 increases in terms of cell-cell interactions after infection, it is unlikely that viral infection with
271 FluB or SARS-CoV-2 causes hypermethylation of these regions. Instead, we propose that these
272 hypermethylated regions might represent a predisposition to viral infection or viral replication
273 by indicating an absence or reduced presence of monocytes. This would require further testing
274 in single individuals to directly measure methylation status of vDMRs before and after infection,
275 however the importance of myeloid cells and specifically monocytes in response to these viral
276 infections among infants is clear.

277 **Conclusions**

278 In this work, we establish a catalogue of the methylation response to respiratory viral infection
279 in infants. We find differences in the epigenomic response to different viruses as well as
280 differential responses across the age range. Finally, we demonstrate that an epigenomic
281 signature of monocyte suppression may actually reflect predisposition to infection or viral
282 replication and may account for inter-individual differences in infection propensity and immune
283 response.

284 **Methods**

285 WGBS Sample characteristics

286 Salvage nasal mucosa derived from children presenting with an acute respiratory illness at
287 Children’s Mercy were accessed and collected from pediatric mid-turbinate nasal flocked swabs
288 as part of routine testing for pathogens. Samples were stored in 3ml of Universal Transport
289 Medium where 200ul of each specimen was tested by BioFire respiratory pathogen panel or for
290 SARS-CoV-2 and remaining aliquot was saved in -80C freezer. In the current study and prior to
291 March 2020, samples derived from infants less than 6 months of age were selected across the
292 following groups: Adenovirus positive, Coronavirus OC43 positive, Enterovirus D68 positive,
293 Influenza Type A positive, Influenza Type B, Human metapneumovirus positive, Human
294 Parainfluenza Virus Type 3 positive, Respiratory syncytial virus positive, Rhinovirus positive and
295 Pathogen Panel Negative, respectively. From March 2020, samples were also derived from
296 SARS-CoV-2 positive infants. An additional set of SARS-CoV-2 (20 months and 19 years) and
297 Influenza Type B positive samples (0-6 months, 6-12 months, 12-24 months, 2-5 years) were
298 selected across different age-groups.

299 Specimen Pooling and DNA Isolation

300 Nasal specimens were stored at -80°C and were brought to room temperature before pooling
301 by viral type or age-group if applicable. Before pooling, the specimens were mixed well with
302 gentle pipetting. In total of 100µL from each specimen of the same viral type or age group was
303 removed and pooled together in a 1.5mL tube. Once all specimen aliquots were added to the
304 viral pool, the pool was mixed by pipetting and 200µl was taken from each pool into a new
305 1.5mL tube for DNA isolation. Similarly, single samples (SARS-CoV-2 positive) was mixed by
306 pipetting and 200µl was taken from each sample into a new 1.5mL tube for DNA isolation. DNA
307 was isolated with a DNeasy Blood and Tissue Kit (Qiagen, Cat No. 69504) with the following
308 modifications to kit protocol: 8µL of RNase A was used instead of 4µl during the optional RNase
309 A step and the lysis incubation time at 56°C was increased to at least 3 hours to ensure
310 complete lysis of the specimens. After isolation, the DNA concentration of each sample was
311 determined using a Qubit dsDNA HS Assay Kit (Fisher, Cat No. Q32851).

312 WGBS Library Preparation and Sequencing

313 In total of 100ng of DNA was aliquoted from each sample pool. Unmethylated λDNA was added
314 to each sample at 0.5%w/v and the samples were sheared mechanically using a Covaris LE220-
315 plus system to a length of 350 bp, using the settings recommended by the manufacturer. The
316 sizing was determined by a High Sensitivity D1000 ScreenTape and Reagents (Agilent, Cat. No.
317 5067-5584 and 5067-5585) on the TapeStation platform. Once the input DNA was at the proper
318 fragment size, the samples were concentrated with a SpeedVac to a volume of 20µL. The
319 samples then underwent bisulfite conversion with an EZ DNA Methylation- Gold kit (Zymo, Cat.
320 No. D5006). The samples were eluted off the spin columns with 15µl of low EDTA TE buffer
321 (Swift, Cat. No. 30024) before library preparation.

322 The low-input libraries were prepared using an ACCEL-NGS Methyl-Seq Library kit (Swift,
323 Cat. No. 30024) with a Methyl-Seq Set A Indexing Kit (Swift, Cat. No. 36024), following the
324 protocol associated with the library kit. During the protocol, bead cleanup steps were
325 performed with SPRIselect beads (Beckman Coulter, Cat. No. B23318). Following the
326 recommendation of the kit, 6 PCR cycles were performed to amplify the samples. The final
327 libraries were quantified with a Qubit dsDNA HS Assay Kit and the size was determined by using
328 a BioAnalyzer High Sensitivity DNA Kit (Agilent, Cat. No. 5067-4626). The libraries were then
329 sequenced on the Illumina NovaSeq6000 System using 150bp paired-end sequencing.

330 WGBS data processing

331 WGBS data was processed using the Epigenome Pipeline available from the DRAGEN Bio-IT
332 platform (Edico Genomics/Illumina). Sequence reads were demultiplexed into FASTQ files using
333 Illumina's bcl2Fastq2-2.19.1 software and trimmed for quality (phred33 \geq 20) and Illumina
334 adapters using trimgalore v.0.4.2 (<https://github.com/FelixKrueger/TrimGalore>). Reads were
335 then aligned to the bisulfite-converted GRCh37 reference genome using DRAGEN EP v2.6.3 in
336 paired-end mode using the directional/Lister methylation protocol presets. Alignments were
337 calculated for both Watson and Crick strands and the highest quality unique alignment was
338 retained. Duplicated reads were removed using picard v 2.17.8 (Broad Institute 2019). A
339 genome-wide cytosine methylation report was generated by DRAGEN to record counts of
340 methylated and unmethylated cytosines at each cytosine position in the genome. Methylation
341 counts were provided for the CpG, CHG and CHH cytosine contexts but only CpG was
342 considered in the study. To avoid potential biases in downstream analyses, CpGs were further
343 filtered by removing CpGs: covered by five or less reads, and located within genomic regions

344 that are known to have anomalous, unstructured, high signal/read counts as reported in DAC
345 blacklisted regions (DBRs) or Duke excluded regions (DERs) generated by the ENCODE project
346 (Amemiya et al. 2019).

347 Differential Methylation Analysis

348 Filtered methylation data from all nasal samples derived from infants were merged, and only
349 CpGs covered by at least 10 reads were kept. The Fisher's exact test for a 2x2 contingency table
350 was used to evaluate the difference in methylated vs. unmethylated reads in the viral sample
351 compared to the matching negative control at each CpG sites. Consecutive nominally significant
352 CpGs ($p < 0.01$) were grouped together into blocks when having the same direction of effect
353 and within 250bp of the adjacent CpG and only region with three or more CpGs were kept for
354 further analysis.

355 Annotation of regulatory elements

356 DNase I Hypersensitive Site (DHS) coordinates were accessed from
357 <https://zenodo.org/record/3838751#.YEY9qRBKhTZ> using 16 different vocabulary
358 representatives as outlined in (Meuleman et al. 2020)

359 Transcription Factor Binding Analysis

360 Transcription factor binding site (TFBS) motif analysis was performed using the Homer software
361 (HOMER findMotifsGenome.pl v4.11.1) (Burger et al. 2013) using the central 200bp of regions.
362 The UMRs and LMRs called from the merged superset sample of all viral pools were used the
363 background.

364 scRNA-seq Patient Recruitment

365 All study subjects were enrolled at Children’s Mercy either using salvage sample collection
366 protocol or using prospective cohort study protocols. Specifically, the NM cohort of control
367 individuals included patients tested for COVID-19 as a part of their standard of care procedure,
368 these samples were collected using a salvage sample protocol (IRB # STUDY00001258).
369 Similarly, patients undergoing multiplex testing for respiratory viruses were regularly screened
370 and all children positive for Influenza B were selected for the NM cohort of Influenza B positive
371 children these samples were collected using salvage sample protocol (IRB # STUDY00001193).
372 For COVID-19 positive children, families were enrolled in the CODIEFY study approved by the
373 Institute Review Board (IRB) at Children’s Mercy (IRB # STUDY00001317). Parents or legally
374 appointed representatives of COVID-19 positive children were approached for enrollment and
375 verbal consent within 24-48 hours of their test results, and children aged 7 years and above
376 have given verbal informed assent. Respiratory specimens were collected and transported by a
377 home-health care nurse following standard precautions within the next 24-48 hours. Samples
378 were processed for nasal cell isolation within 2 - 4 hours of collection.

379 Single-cell RNA-sequencing

380 Samples were collected from pediatric mid-turbinate nasal flocked swabs and were stored in
381 3ml of Universal Transport Medium where 200ul of each specimen was tested by BioFire
382 respiratory pathogen panel or for SARS-CoV-2 and remaining aliquot was kept in 4C until test
383 result was available (within 12h). 1ml of each sample was diluted with cold PBS (Thermo Fisher
384 Cat No. 14190144) + 2% FBS (GE Healthcare Cat No. SH30088.03HI) up to a total volume of 5 mL
385 and passed through a 40- μ m nylon mesh cell strainer that had been prewetted with 2 mL of
386 PBS + 2% FBS. The strainer was then rinsed with 7 mL of cold PBS + 2% FBS. The sample was

387 transferred to a 15-mL conical tube and centrifuged at 300 x g at 4°C for 8 minutes. The
388 supernatant was carefully removed without disturbing the cell pellet. The cell pellet was
389 resuspended in 200 µL of cold PBS + 2% FBS, and the cell count and viability were assessed
390 using 0.4% Trypan Blue and a Countess II automated cell counter. The cell suspension was
391 transferred to a 1.5-mL tube and centrifuged at 300 x g at 4°C for 8 minutes, and the
392 supernatant was carefully removed without disturbing the cell pellet. The cell pellet was
393 resuspended in 1 mL of cold Recovery Cell Culture Freezing Medium (Thermo Fisher Cat No.
394 12648010), and the cell suspension was transferred to a cryogenic storage vial. The cryogenic
395 storage vial was placed in a Corning CoolCell FTS30, which was then placed in a -80°C freezer
396 overnight. Samples were stored at -80°C for no longer than one week before being thawed and
397 processed for scRNAseq. Upon thawing, sample with less than 30% viability were excluded from
398 analysis and cells were used in pools or individually. For the Influenza B positive samples, a
399 single pool of four samples was created (4-11 years, n=4). COVID-19 positive samples (5-11
400 years, n=3) were processed individually. For each sample to be thawed, 10 mL of Thawing
401 Medium consisting of DMEM/F-12 (Thermo Fisher Cat No. 11320033) supplemented with 10%
402 FBS and 100 units/mL of penicillin and 100 µg/mL of streptomycin (Thermo Fisher Cat No.
403 15140122) was prewarmed in a 37°C bead bath. Each cryogenic storage vial containing a
404 sample to be thawed was placed in the 37°C bead bath. No more than 5 samples were thawed
405 at a time. When only a small ice crystal remained in the sample, both the cryogenic storage vial
406 and the 15-mL conical tube containing the Thawing Medium were aseptically transferred to the
407 biosafety cabinet. 1 mL of Thawing Medium was slowly added, dropwise, to the sample. The
408 diluted sample was then mixed gently by pipetting and further diluted in the remaining 9 mL of

409 Thawing Medium. The thawed and diluted cells were left at room temperature while the
410 remaining samples were similarly thawed. When all samples in the batch were thawed, the
411 samples were centrifuged at 300 x *g* for 8 min. The supernatant was carefully removed without
412 disturbing the cell pellets. The cell pellets were each resuspended in 0.5 mL of Thawing
413 Medium, and the cell suspensions were placed on ice. Each pool or individual sample was
414 passed through a prewetted 40- μ m nylon mesh cell strainer, and the cell strainers were rinsed
415 with 5 mL of cold Thawing Medium. The pooled or individual sample cell suspensions were
416 centrifuged at 300 x *g* for 8 min at 4°C, and the supernatant was carefully aspirated without
417 disturbing the cell pellets. The cell pellets were resuspended in 100 μ L of cold Thawing Medium,
418 and cell count and viability were assessed using 0.4% Trypan Blue and a Countess II automated
419 cell counter. For the Influenza B group, 2 wells of a Chromium Chip B (10x Genomics Cat No.
420 1000153) were loaded with 32,000 cells each; for each SARS-CoV-2 positive sample, 2 wells of a
421 Chromium Chip B (10x Genomics Cat No. 1000153) were loaded with 16,000 cells each.
422 Following cell loading, scRNAseq was performed identically for all samples using the Chromium
423 Single Cell 3' Library & Gel Bead Kit v3 (10x Genomics Cat No. 1000075) according to the
424 manufacturer's protocol. Sequencing was performed using an Illumina NovaSeq 6000. Runs of
425 WGBS were 2x151 cycle paired-end, while runs of scRNAseq were 2x94 cycle paired-end.

426 Post-sequencing analysis scRNAseq

427 Sequenced reads were initially processed by the cellranger pipeline (v3.1.0) which includes
428 fastq creation, read alignment, gene counting, and cell calling. All samples were mapped to the
429 cellranger GRCh38 v1.2.0 genome. The resulting cell by gene matrix from the cellranger "count"
430 step was then processed using standard workflows in Seurat (Butler et al. 2018; Stuart et al.

431 2019). In brief, low quality cells were removed by filtering out cells with a unique gene count
432 lower than 750 and more than 50% mitochondrial reads. The gene counts for remaining cells
433 that passed quality control were then normalized using SCTransform (Hafemeister and Satija
434 2019) with the replicate captures as a batch variable. The COVID-19 positive and Influenza B
435 positive samples, were normalized independently, and integrated with the control samples
436 using the FindIntegrationAnchors and IntegratedData functions in Seurat with default
437 parameters. The integrated data was then used for linear and non-dimensional reduction,
438 nearest neighbor finding, and unsupervised clustering. Cell types were assigned by examining
439 expression of known genes in the unsupervised clusters, as well as examining markers of the
440 clusters identified using the FindAllMarkers function in Seurat with default parameters.

441 Cell-cell interaction quantification

442 We quantified the interactions between different cell types in the nasal epithelia of pediatric
443 patients using the cellphoneDB program (Efremova et al. 2020). The SCTransform corrected
444 gene expression values for each infection state were independently input into cellphoneDB
445 using the “statistical analysis” pipeline. The resulting cell-type by cell-type matrix of statistically
446 significant interactions for each infection state were then plotted as clustered heatmaps, using
447 a consistent color scale between the different infection states.

448 Gene expression module scoring

449 Gene expression modules for Interferon stimulated genes and cell death markers were scored
450 using the AddModuleScore function in Seurat. The genes used for each of these modules can be
451 found in Supplementary Table 8.

452 **Abbreviations**

453 SARS-CoV-2: Severe acute respiratory syndrome – Coronavirus – 2

454 FluB: Influenza Type B

455 FluA: Influenza Type A

456 DMR: differentially methylated region

457 vDMR: viral differentially methylated region

458 ARI: acute respiratory illness

459 WGBS: whole genome bisulfite sequencing

460 TFBS: Transcription factor binding site

461 Adeno: Adenovirus

462 Corona Oc43

463 EVD68: Enterovirus D68

464 hMPV: Human metapneumovirus

465 PIV3: Human Parainfluenza Virus Type 3

466 RSV: Respiratory syncytial virus

467 REV: Rhino(entro)virus

468 GWAS: Genome-wide association study

469 scRNAseq: single-cell RNA-sequencing

470 **Declarations**

471 Ethics approval and consent to participate

472 The complete WGBS project and single-cell profiling using pooled samples was determined as

473 non-human subjects research by the Institutional Review Board (IRB) at Children’s Mercy

474 Research Institute. Single sample single-cell profiling (SARS-CoV-2) study was approved by the
475 IRB (STUDY00001317) at Children’s Mercy Research Institute.

476 Consent for publication

477 All study participants and their family members enrolled in human subjects’ research (i.e.
478 single-cell profiling of SARS-CoV-2 positive nasal samples) provided informed consent for
479 publication.

480 Availability of data and materials

481 All raw and processed sequencing data generated in this study have been submitted to the
482 NCBI Gene Expression Omnibus (GEO; <https://www.ncbi.nlm.nih.gov/geo/>) under accession
483 number GSE168254 and GSE162864. Fully processed single-cell data are available for
484 exploration through the UCSC cell browser (lifefspan-nasal-atlas.cells.ucsc.edu)

485 Competing interests

486 The authors declare that they have no competing interests

487 Funding

488 This work was supported by a CTSA grant from National Institute of Health (NIH)/NCATS
489 awarded to the University of Kansas for Frontiers: University of Kansas Clinical and Translational
490 Science Institute (# UL1TR002366). Research reported in this publication was also supported by
491 the National Institute On Minority Health And Health Disparities of the NIH under Award
492 Number R01MD015409. The content is solely the responsibility of the authors and does not
493 necessarily represent the official views of the NIH. This work was also supported by grants from
494 Children’s Mercy Research Institute awarded to RS, TP and EG. E.G. holds the Roberta D.

495 Harding & William F. Bradley, Jr. Endowed Chair in Genomic Research and T.P. holds the Dee
496 Lyons/Missouri Endowed Chair in Pediatric Genomic Medicine.

497 Authors' contributions

498 EG, RS, and TP conceived the study. KW, BK, and WC analyzed data. RS and DB provided
499 samples. KW, and EG prepared the manuscript with significant contribution by TP and RS. All
500 authors read and approved the manuscript.

501 Acknowledgments

502 We thank Bradley Belden, Rebecca Biswell, Daniel Louiselle, Nyshela Posey and Margaret
503 Gibson at the Genomic Medicine Center at Children's Mercy Kansas City for technical assistance
504 and clinical coordination.

505 **References**

506 Allum F, Hedman ÅK, Shao X, Cheung WA, Vijay J, Guénard F, Kwan T, Simon MM, Ge B, Moura
507 C, et al. 2019. Dissecting features of epigenetic variants underlying cardiometabolic risk
508 using full-resolution epigenome profiling in regulatory elements. *Nature Communications*
509 **10**.

510 Allum F, Shao X, Guénard F, Simon MM, Busche S, Caron M, Lambourne J, Lessard J, Tandre K,
511 Hedman ÅK, et al. 2015. Characterization of functional methylomes by next-generation
512 capture sequencing identifies novel disease-associated variants. *Nature Communications*
513 **6**.

514 Amemiya HM, Kundaje A, Boyle AP. 2019. The ENCODE Blacklist: Identification of Problematic
515 Regions of the Genome. *Scientific Reports* **9**.

516 Broad Institute. 2019. Picard toolkit. <http://broadinstitute.github.io/picard/>.

- 517 Burger L, Gaidatzis D, Schübeler D, Stadler MB. 2013. Identification of active regulatory regions
518 from DNA methylation data. *Nucleic Acids Research* **41**.
- 519 Busche S, Shao X, Caron M, Kwan T, Allum F, Cheung WA, Ge B, Westfall S, Simon MM, Barrett
520 A, et al. 2015. Population whole-genome bisulfite sequencing across two tissues highlights
521 the environment as the principal source of human methylome variation. *Genome Biology*
522 **16**.
- 523 Butler A, Hoffman P, Smibert P, Papalexi E, Satija R. 2018. Integrating single-cell transcriptomic
524 data across different conditions, technologies, and species. *Nature Biotechnology* **36**.
- 525 Collins PL, Fearn R, Graham BS. 2013. Respiratory syncytial virus: Virology, reverse genetics,
526 and pathogenesis of disease. *Current Topics in Microbiology and Immunology* **372**: 3–38.
- 527 Efremova M, Vento-Tormo M, Teichmann SA, Vento-Tormo R. 2020. CellPhoneDB: inferring
528 cell–cell communication from combined expression of multi-subunit ligand–receptor
529 complexes. *Nature Protocols* **15**.
- 530 Grundberg E, Meduri E, Sandling JK, Hedman ÅK, Keildson S, Buil A, Busche S, Yuan W, Nisbet J,
531 Sekowska M, et al. 2013. Global analysis of dna methylation variation in adipose tissue
532 from twins reveals links to disease-associated variants in distal regulatory elements.
533 *American Journal of Human Genetics* **93**: 876–890.
- 534 Hafemeister C, Satija R. 2019. Normalization and variance stabilization of single-cell RNA-seq
535 data using regularized negative binomial regression. *Genome Biology* **20**.
- 536 Liang L, Willis-Owen SAG, Laprise C, Wong KCC, Davies GA, Hudson TJ, Binia A, Hopkin JM, Yang
537 I v., Grundberg E, et al. 2015. An epigenome-wide association study of total serum
538 immunoglobulin e concentration. *Nature* **520**: 670–674.

- 539 Lu R, Zhao X, Li J, Niu P, Yang B, Wu H, Wang W, Song H, Huang B, Zhu N, et al. 2020. Genomic
540 characterisation and epidemiology of 2019 novel coronavirus: implications for virus origins
541 and receptor binding. *The Lancet* **395**: 565–574.
- 542 Maeda M, Moro H, Ushijima T. 2017. Mechanisms for the induction of gastric cancer by
543 *Helicobacter pylori* infection: aberrant DNA methylation pathway. *Gastric Cancer* **20**: 8–15.
- 544 Matsusaka K, Funata S, Fukuyo M, Seto Y, Aburatani H, Fukayama M, Kaneda A. 2017. Epstein–
545 Barr virus infection induces genome-wide de novo DNA methylation in non-neoplastic
546 gastric epithelial cells. *Journal of Pathology* **242**: 391–399.
- 547 Mcerlean P, Favoreto S, Costa FF, Shen J, Quraishi J, Biyasheva A, Cooper JJ, Scholtens DM,
548 Vanin EF, de Bonaldo MF, et al. 2014. *Human rhinovirus infection causes different DNA*
549 *methylation changes in nasal epithelial cells from healthy and asthmatic subjects.*
550 <http://www.biomedcentral.com/1755-8794/7/37>.
- 551 Meuleman W, Muratov A, Rynes E, Halow J, Lee K, Bates D, Diegel M, Dunn D, Neri F,
552 Teodosiadis A, et al. 2020. Index and biological spectrum of human DNase I hypersensitive
553 sites. *Nature* **584**: 244–251.
- 554 Norlander AE, Peebles RS. 2020. Innate type 2 responses to respiratory syncytial virus infection.
555 *Viruses* **12**.
- 556 Okano M, Bell DW, Haber DA, Li E. 1999. *DNA Methyltransferases Dnmt3a and Dnmt3b Are*
557 *Essential for De Novo Methylation and Mammalian Development.*
- 558 Shi T, McAllister DA, O’Brien KL, Simoes EAF, Madhi SA, Gessner BD, Polack FP, Balsells E, Acacio
559 S, Aguayo C, et al. 2017. Global, regional, and national disease burden estimates of acute

560 lower respiratory infections due to respiratory syncytial virus in young children in 2015: a
561 systematic review and modelling study. *The Lancet* **390**: 946–958.

562 Smith ZD, Chan MM, Mikkelsen TS, Gu H, Gnirke A, Regev A, Meissner A. 2012. A unique
563 regulatory phase of DNA methylation in the early mammalian embryo. *Nature* **484**: 339–
564 344.

565 Stec DS, Hill lii MG, Collins’ PL. 1991. *Sequence Analysis of the Polymerase L Gene of Human*
566 *Respiratory Syncytial Virus and Predicted Phylogeny of Nonsegmented Negative-Strand*
567 *Viruses*.

568 Stuart T, Butler A, Hoffman P, Hafemeister C, Papalexi E, Mauck WM, Hao Y, Stoeckius M,
569 Smibert P, Satija R. 2019. Comprehensive Integration of Single-Cell Data. *Cell* **177**: 1888-
570 1902.e21.

571 Stunnenberg HG, Abrignani S, Adams D, de Almeida M, Altucci L, Amin V, Amit I, Antonarakis SE,
572 Aparicio S, Arima T, et al. 2016. The International Human Epigenome Consortium: A
573 Blueprint for Scientific Collaboration and Discovery. *Cell* **167**: 1145–1149.

574 Szabo A, Rajnavolgyi E. 2014. Finding a fairy in the forest: ELF4, a novel and critical element of
575 type I interferon responses. *Cellular and Molecular Immunology* **11**: 218–220.

576 Tsaprouni LG, Yang TP, Bell J, Dick KJ, Kanoni S, Nisbet J, Viñuela A, Grundberg E, Nelson CP,
577 Meduri E, et al. 2014. Cigarette smoking reduces DNA methylation levels at multiple
578 genomic loci but the effect is partially reversible upon cessation. *Epigenetics* **9**: 1382–1396.

579 Vuckovic D, Bao EL, Akbari P, Lareau CA, Mousas A, Jiang T, Chen MH, Raffield LM, Tardaguila
580 M, Huffman JE, et al. 2020. The Polygenic and Monogenic Basis of Blood Traits and
581 Diseases. *Cell* **182**: 1214-1231.e11.

582 Ygberg S, Nilsson A. 2012. The developing immune system - From foetus to toddler. *Acta*
583 *Paediatrica, International Journal of Paediatrics* **101**: 120–127.

584 You F, Wang P, Yang L, Yang G, Zhao YO, Qian F, Walker W, Sutton R, Montgomery R, Lin R, et
585 al. 2013. ELF4 is critical for induction of type I interferon and the host antiviral response.
586 *Nature Immunology* **14**: 1237–1246.

587 Zhang X, Zhivaki D, Lo-Man R. 2017. Unique aspects of the perinatal immune system. *Nature*
588 *Reviews Immunology* **17**: 495–507.

589

590 **Figure legends:**

591 Figure 1: Hierarchical clustering of top 50% variable CpGs in nasal samples derived from ten
592 respiratory viral infections.

593 Figure 2: Respiratory viruses elicit differential magnitude and direction of host methylation
594 response. A) Discovery rate of vDMR. hMPV, N=496; RV, N=665; Adeno, N=943; Corona (Oc43),
595 N=1281; EVD68, N=3129; FluA, N=3439; PIV3, N=4788; RSV, N=12557; FluB, N=14361; and
596 SARS-CoV-2, N=78542. B) Methylation status of vDMR

597 Figure 3: FluB and SARS-CoV-2 infection are associated with differential responses of epithelial
598 and immune methylomes. A) Fold change compared to control sample of presence of regions
599 annotated to specific cell lineages in replicated vDMR sets. B) Fold change compared to control
600 sample of presence of genomic regions annotated to specific immune cell lineages in
601 hypermethylated vDMR for FluB and SARS-CoV-2. C) $-\log_{10}$ p-value fisher's exact test for a
602 positive association between infection and presence of genomic regions annotated to specific
603 immune lineages in hypermethylated vDMR. Dashed line represents p-value of 0.05.

604 Figure 4: Functional analysis of replicated vDMR in adolescent infection. A) UMAP projection of
605 cells obtained from pooled adolescent nasal mucosa samples infected with FluB, SARS-CoV-2
606 and uninfected age-matched controls. B-C) Expression level of genes “modules” derived from
607 genes nearest vDMR for Flu B (B) and SARS-CoV-2 (C). D) Percent of total cells in each cell type
608 for uninfected and infected pooled samples. E) Heatmaps of cell-cell interactions between all
609 cell types for FluB infected, SARS-CoV-2 infected, and uninfected controls.

610 Supplementary Figure 1: Enrichment of regulatory element annotations of hyper (A) and hypo
611 (B) vDMR. Fold change shown is compared to control sample.

612 Supplementary Figure 2: Enrichment of regulatory element annotations of RSV hypo vDMR.
613 Fold change shown is compared to control sample.

614 Supplementary Figure 3: Density plots of methylation level across discovery and replication set
615 for SARS-CoV-2 (A) and Flu B (B).

616 Supplementary Figure 4: FluB and SARS-CoV-2 hypermethylated vDMR are nearest genes that
617 are enriched for innate immune cell development terms. A-B) GO term enrichment for genes
618 that are nearest hypermethylated vDMRs for SARS-CoV-2 (A) and FluB (B). C-D) Expression
619 domain enrichment for genes that are nearest hypermethylated vDMRs for SARS-CoV-2 (C) and
620 FluB (D).

621 Supplementary Figure 5: Expression of *ELF4* in different cell lineages present in venous blood
622 demonstrates enrichment in monocytes.

623 Supplementary Figure 6: Genomic regions associated with monocyte development determined
624 by GWAS are the most significantly enriched regions in hypermethylated vDMR for FluB and
625 SARS-CoV-2.

626 Supplementary Figure 7: Monocytes repeatably increase cell-cell interactions after infection. A-
627 B) Change in number of interactions between each cell-type pair after infection with SARS-CoV-
628 2 (A), and Flu B (B). Solid line represents a p-value of 0.05.

Figure 1

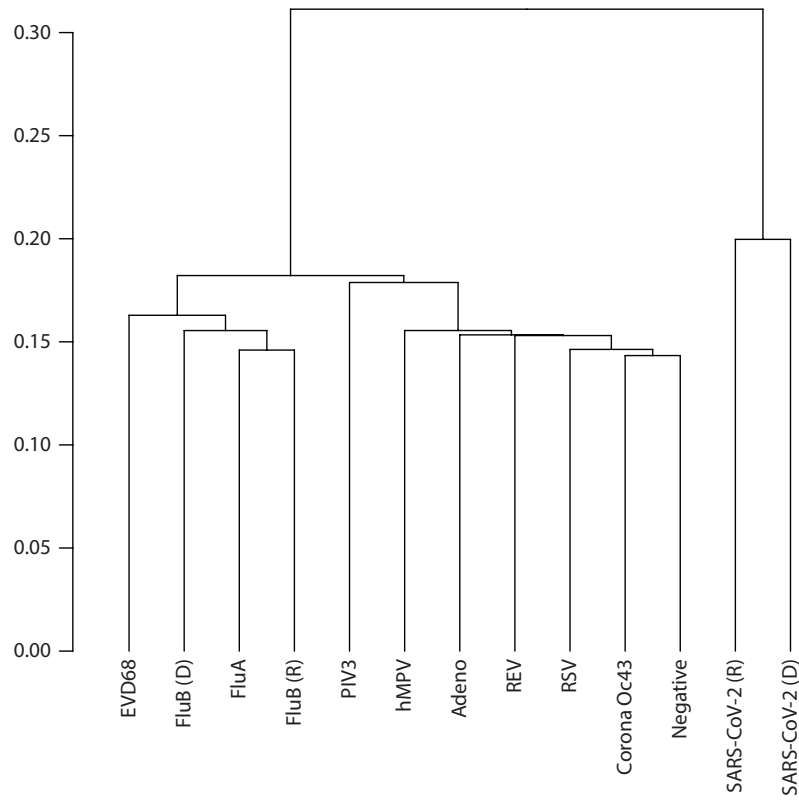


Figure 2

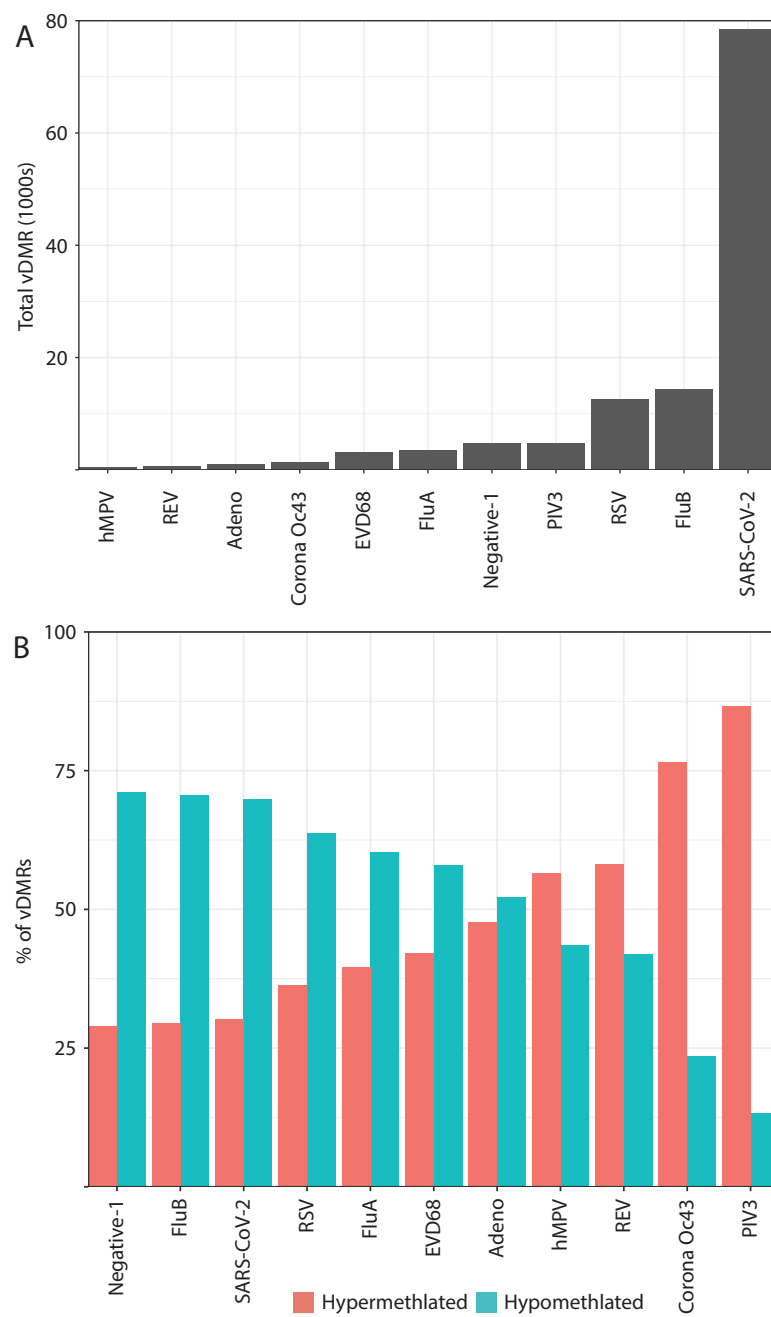


Figure 3

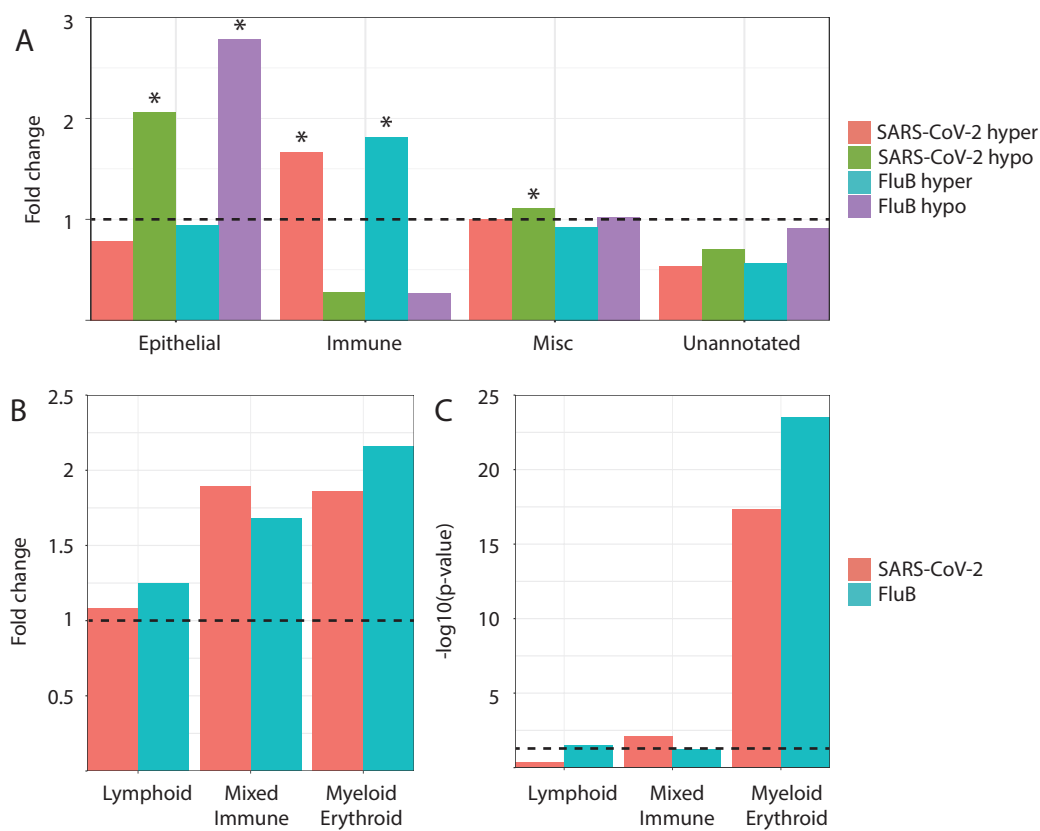
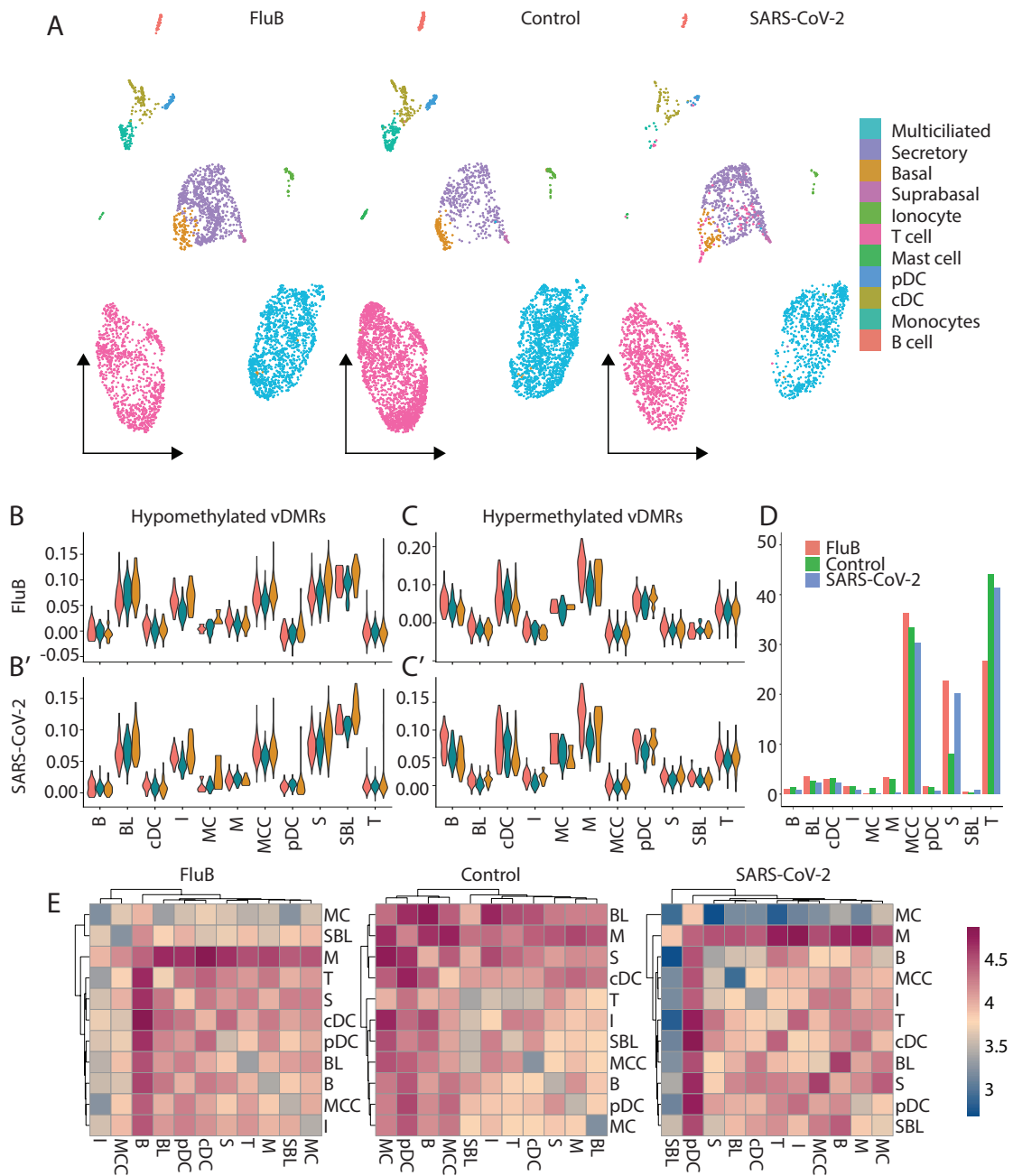
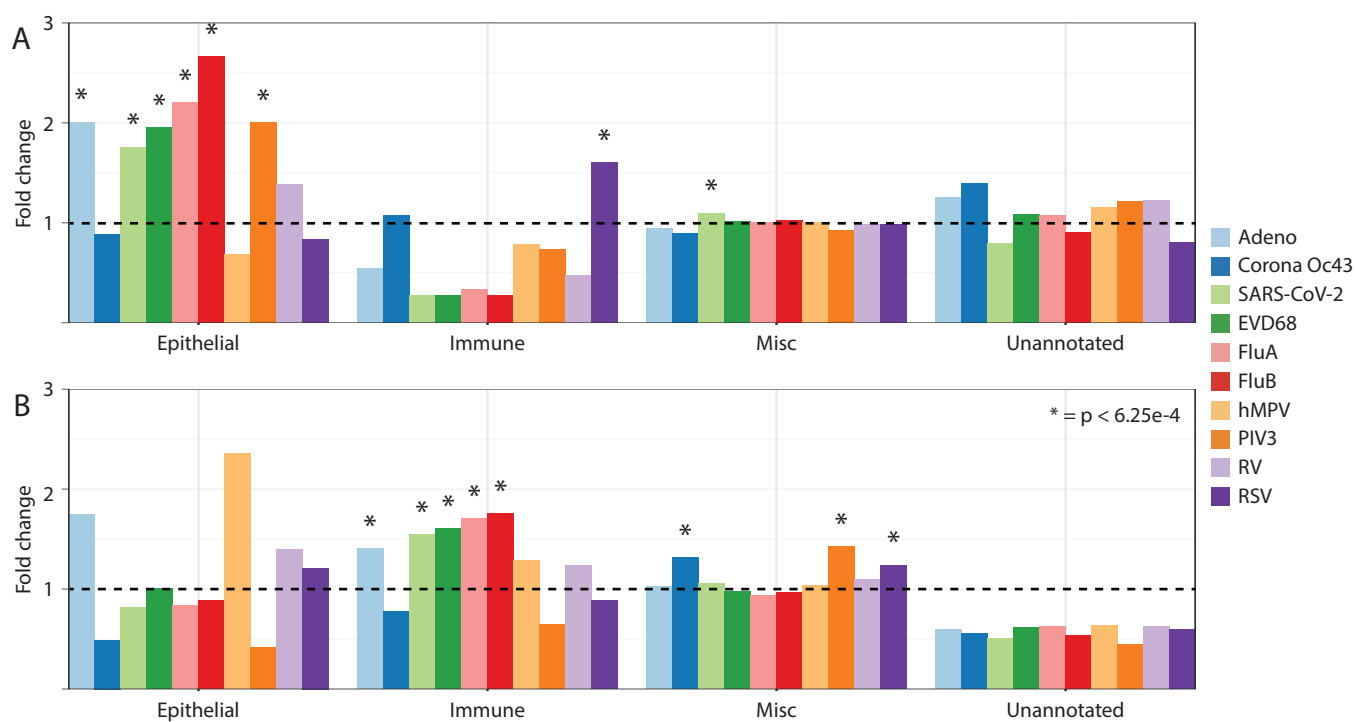


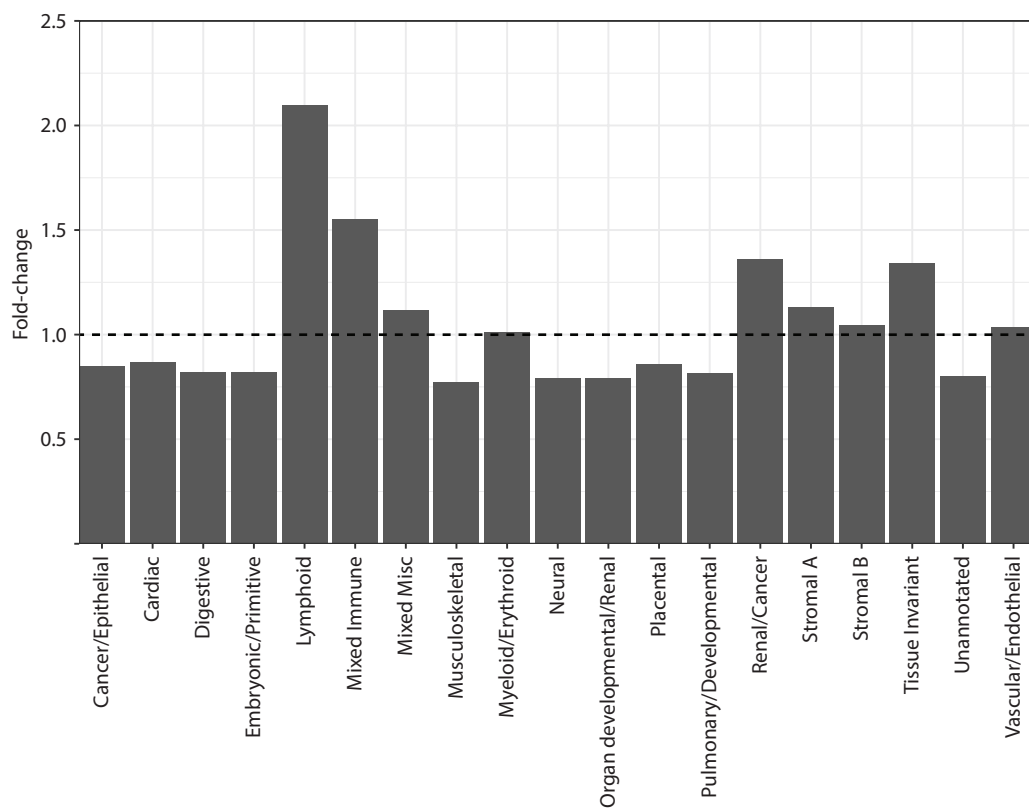
Figure 4



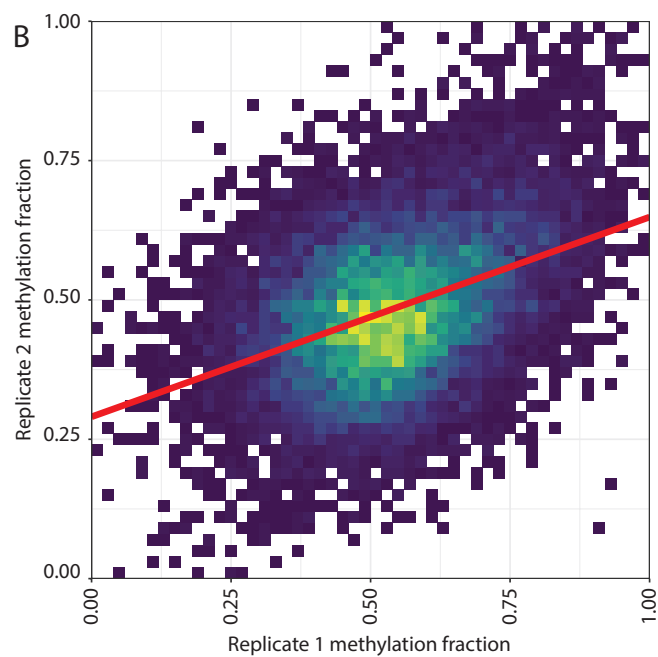
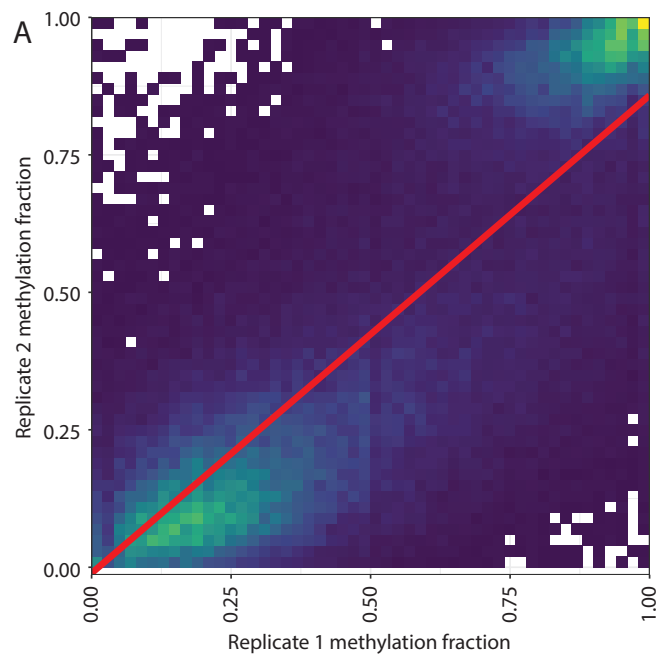
Supplementary Figure 1



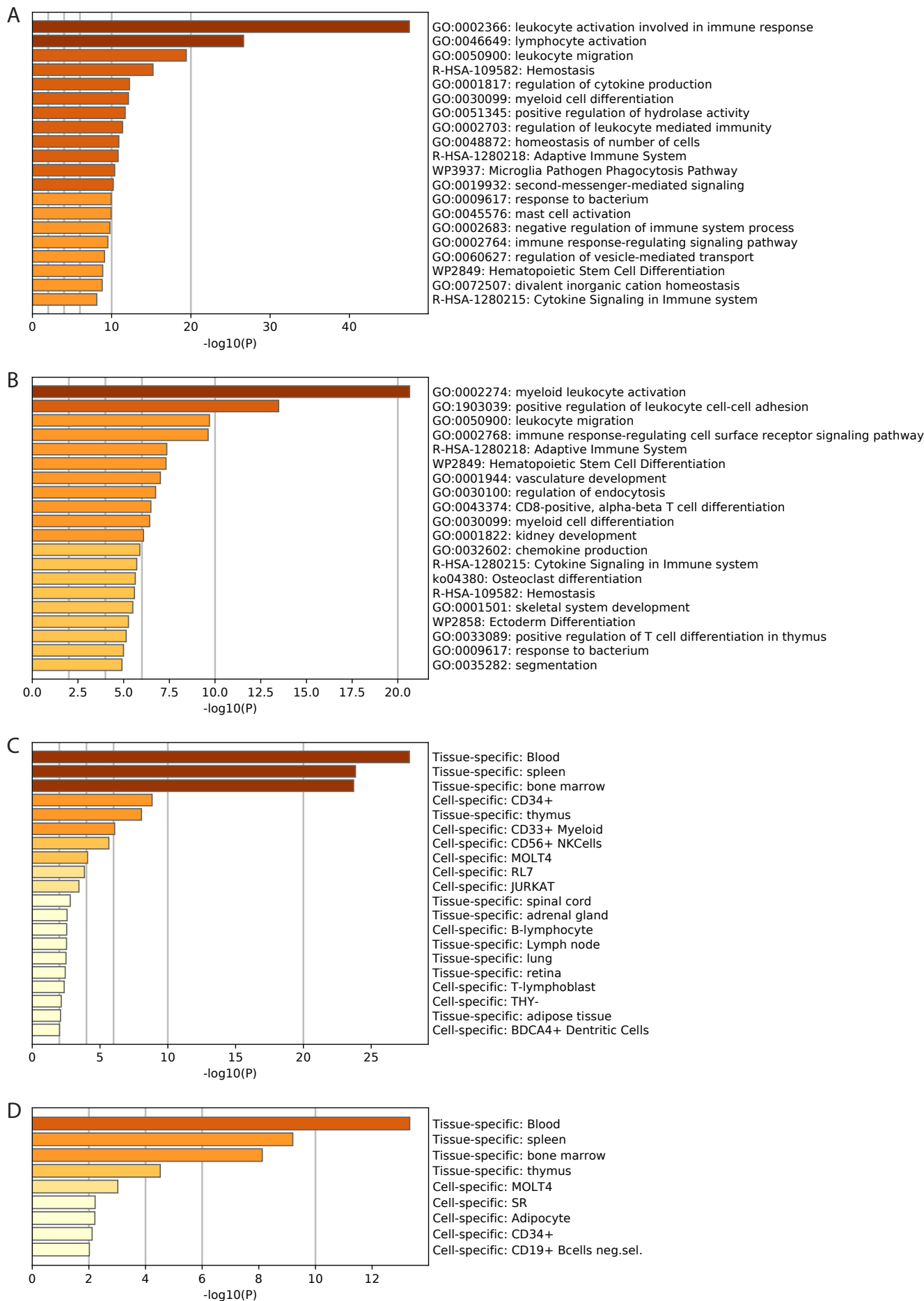
Supplementary Figure 2



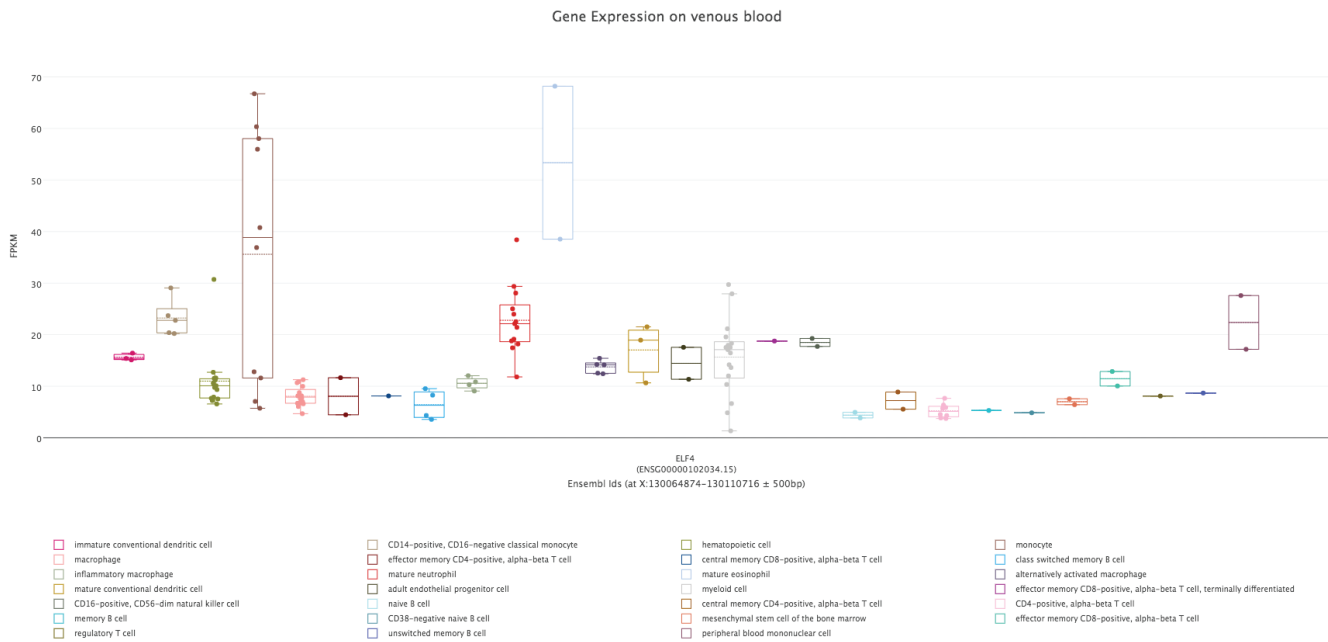
Supplementary Figure 3



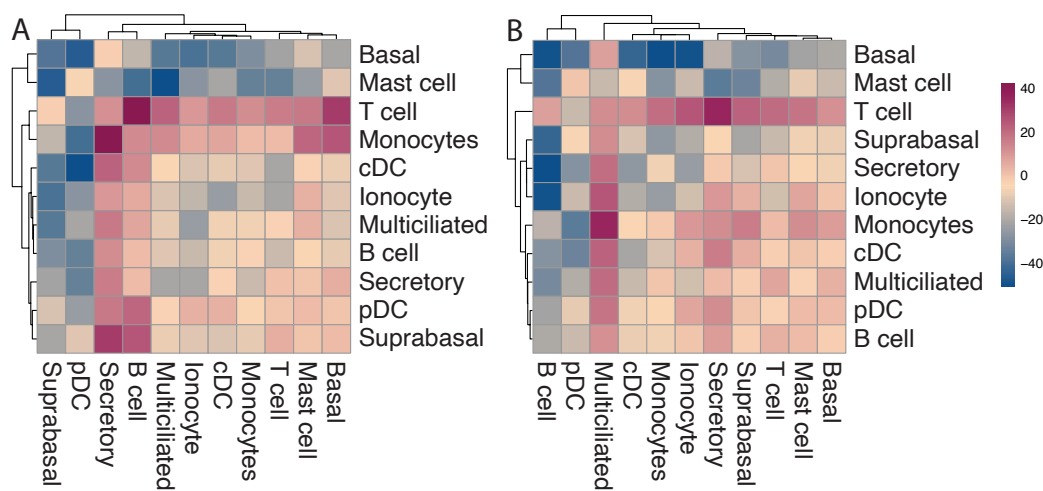
Supplementary Figure 4



Supplementary Figure 5



Supplementary Figure 6



Supplementary Figure 7

